



ATLAS Note

ATL-COM-UPGRADE-2023-09

28th July 2023



Draft version 0.1

1

Background noise reduction with HGTD for the search of LLPs

2

Leo Reynaud (Student)^a and Louie D.Corpé ^a

3

^a*LPC Clermont-Ferrand*

4

This five-month internship aims to analyze the impact of adding the HGTD detector during the future Run 4 of the Large Hadron Collider (LHC) in the search for Long-Lived Particles (LLPs). The analysis focuses on the fraction of the signal that HGTD captures with its location and its potential to effectively reject certain background noises, such as Beam-Induced Background (BIB), which can closely resemble LLP signals during their detections. The obtained results have shown that the presence of HGTD in the forward regions reduces the impact of BIB on LLP detection. Significant improvements in BIB rejection efficiency have been observed when it propagates opposite to the particles coming from the interaction point. However, further analysis is still required for the scenario where BIB propagates in the same direction as the particles.

16 © 2023 CERN for the benefit of the ATLAS Collaboration.

17 Reproduction of this article or parts of it is allowed as specified in the CC-BY-4.0 license.

18 **Contents**

19	Introduction	4
20	I Part 1: Getting Started.	5
21	1 ATLAS and the LHC	5
22	1.1 The LHC	5
23	1.2 ATLAS	6
24	1.3 The Coordinate System in ATLAS	7
25	1.4 Detectors in ATLAS	7
26	1.5 The HL-LHC and its Future Detectors	10
27	2 LLPs (Long-Lived Particles)	10
28	3 Backgrounds for LLP Searches	12
29	3.1 Different Backgrounds in ATLAS	12
30	3.2 The Beam-Induced Background (BIB)	13
31	3.3 Pileup	13
32	II Appendices	14
33	4 Signal Study in the HGTD Region	14
34	4.1 The Samples	14
35	4.2 Calculation of Acceptance for Different Samples	14
36	4.3 Weighting Formula	15
37	4.4 Acceptance for Different Lifetimes	16
38	4.5 Analysis of Results	16
39	III BIB Rejection	17
40	5 Objective	17
41	6 Athena, the Software of ATLAS	18
42	7 Simulation Steps	19
43	7.1 Available Variables	19
44	8 Samples	20
45	8.1 BIB Samples	21
46	8.2 Top Samples	21
47	8.3 Minbias Samples	22
48	8.4 Visualization	22
49	9 Final Samples	22

50	10 Clustering with Anti-KT	23
51	10.1 The Energy-Momentum Four-Vector	23
52	10.2 The Optimal Radius	24
53	11 Clustering with DBSCAN	25
54	11.1 Reason for a second clustering	25
55	11.2 DBSCAN	25
56	12 Linear Fit with Minuit	26
57	13 Analysis	27
58	14 Results	27
59	15 Conclusion	28
60	IV Appendices	31
61	16 Signal Study in the HGTD Region	31
62	16.1 The Samples	31
63	16.2 Calculation of Acceptance for Different Samples	31
64	16.3 Weighting Formula	32
65	16.4 Acceptance for Different Lifetimes	33
66	16.5 Analysis of Results	33

67 Introduction

68 Particle physics is a fascinating field of research that explores the foundations of our universe at its most
 69 fundamental scale. However, despite remarkable advances over the past decades, there are still many
 70 challenges and unresolved issues that continue to pique interest and curiosity.

71 Indeed, current theories, such as the Standard Model of particle physics, do not provide a complete
 72 description of the universe. Fundamental questions concerning topics like dark matter, dark energy, matter-
 73 antimatter asymmetry, quantum gravity, and the unification of fundamental forces remain unanswered.
 74 Therefore, there is a need to explore new theoretical perspectives that address these issues. It is in
 75 this particular context that Long-Lived Particles (LLPs) are envisioned, representing particles with long
 76 lifetimes and extremely weak interactions with matter.

77 Several methods have been developed to search for LLPs and study their properties. One of the most
 78 common approaches involves utilizing particle detectors within large particle accelerators, such as the
 79 ATLAS detector at the LHC. These detectors are designed to identify and measure the properties of
 80 particles produced during high-energy collisions. Indirect detection techniques are predominantly used in
 81 these searches. Instead of directly detecting the LLPs themselves, researchers look for indirect signatures
 82 of their presence. This can include searching for energy imbalances, isolated jets, or other anomalies in
 83 experimental data. The search for LLPs, therefore, involves the study of unusual signals, such as particle
 84 tracks traveling over long distances before decaying or abnormally high energy deposits [1].

85 During Run 4 of the LHC, new detectors will be available, potentially allowing for more extensive analyses.
 86 ATLAS will be enhanced by the presence of a new tracker, and the addition of the HGTD detector in the
 87 forward region of ATLAS will enable much more efficient observations in a specific zone of the detector.
 88 In this study, we will explore the possibilities these new detectors will offer for LLP research when they
 89 come into operation.

Abréviation	Mot complet
ATLAS	A Toroidal LHC ApparatuS
LHC	Large Hadron Collider
HGTD	High Ganularity Timing Detector
HL-LHC	High-Luminosity LHC
LLP	Long Lived Particle
BIB	Beam Induced Background
HCal	Hadronique Calorimetre
ECal	Electromagnetique Calorimetre
FCal	Forward Calorimetre
IBL	Insertable B-Layer
SCT	SemiConducteur Tracker
PS	Proton Synchrotron
SPS	Super Proton Synchrotron

Table 1: Tableau des abréviations utilisées dans ce rapport.

Part I

Part 1: Getting Started.

1 ATLAS and the LHC

1.1 The LHC

The LHC is the largest and most powerful particle accelerator in the world. Located at the Franco-Swiss border near Geneva, the LHC has a circumference of 26.659 km and houses four very large detectors: ATLAS, CMS, LHCb, and ALICE, depicted in Figure 1. It operates by accelerating beams of particles to speeds close to that of light. The PS (Proton Synchrotron) is the first link in the LHC's acceleration chain. It receives protons from an ion source and accelerates them to an energy of 25 GeV. Once the protons reach their maximum energy in the PS, they are transferred to the SPS (Super Proton Synchrotron). The SPS, an even larger and more powerful synchrotron, accelerates the protons to an energy of 450 GeV. The SPS acts as a pre-injection accelerator for the LHC, preparing the protons to be injected into the LHC itself. Once accelerated, the LHC collides the particles at a frequency of 2.5 ns. The particles used are mainly protons, but the LHC has also been used for collisions of heavy nuclei. High-energy collisions create conditions similar to those that existed shortly after the Big Bang, allowing us to probe the basic constituents of matter. Since its commissioning, the LHC has been extremely successful, most notably with the discovery of the Higgs boson. Since then, the LHC has continued to produce remarkable scientific results and push the boundaries of our knowledge.???

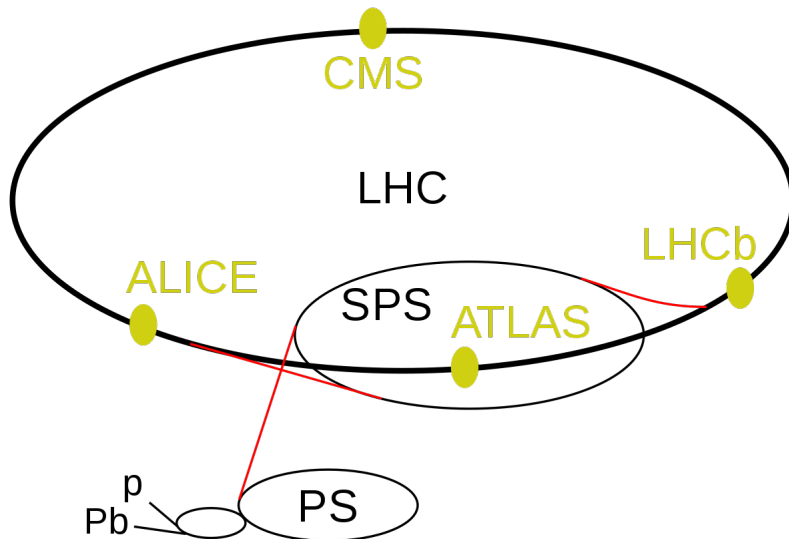


Figure 1: The LHC and its various detectors.

Since its commissioning in 2008, the LHC has undergone various major upgrades, increasing the energy and number of proton collisions and enabling improvements in the different detectors. Each major upgrade is followed by a phase called a "Run." The LHC is currently in Run 3 and is already preparing for Run 4, on

which this study depends. Run 4, also known as the High-Luminosity LHC (HL-LHC), aims primarily to increase the amount of data collected during particle collisions. To achieve this goal, the HL-LHC involves significant improvements to the LHC infrastructure. This includes upgrading the superconducting magnets that guide the particle beams through the accelerator to generate more intense magnetic fields. With these enhancements, the HL-LHC plans to increase the LHC's luminosity by a factor of ten compared to its current performance. This means that the number of particle collisions per second will be significantly increased, providing an unprecedented amount of data for scientific research but also increasing the pileup and thus noise in each event. "Pileup" occurs when there are multiple particle collisions in the same proton beam at the same time. When this happens, the detectors record signals from all collisions, making it challenging to distinguish between signals from interesting events and those from background events. Reducing pileup is possible through improved spatial resolution. Hence, the addition of new, more efficient detectors and the enhancement of existing detectors are essential to maintain efficient data collection.

1.2 ATLAS

Every day, billions of particle collisions occur within the LHC at CERN. One of the flagship experiments conducted there is the ATLAS experiment, which aims to probe the elementary constituents of matter and understand the fundamental mechanisms of our universe.

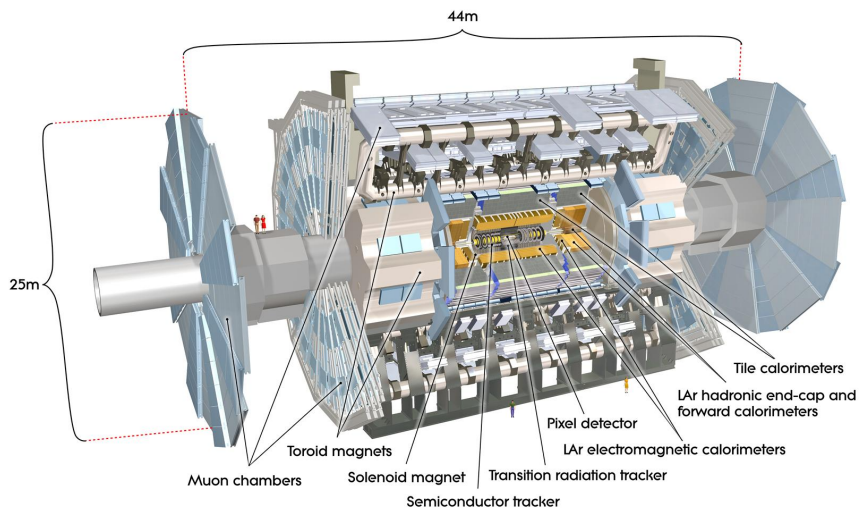


Figure 2: The ATLAS detector.

ATLAS is a cylindrical particle detector that measures 46 meters in length and 25 meters in diameter, as depicted in Figure 2 . It is located at one of the four intersections where the LHC's proton beams cross and is the largest detector at the LHC. The detector is designed to measure collision products of protons with a collision energy of up to 13.6 TeV. It also features a 2 Tesla superconducting magnet to bend the trajectory of charged particles, allowing for the measurement of their momentum.

ATLAS has numerous applications, including the search for new particles, the study of electroweak and strong forces, the measurement of properties of the Higgs boson, and the search for dark matter. The data collected by ATLAS is used to test many physical theories and is used to precisely measure certain fundamental constants.

136 1.3 The Coordinate System in ATLAS

137 In the cylindrical coordinate system of ATLAS, as illustrated in Figure 3, the positions of particles are
 138 specified using several variables. The radius r covers the (x, y) plane and represents the distance between
 139 the particle and the central axis of the detector. The azimuthal angle φ describes the rotation around the
 140 central axis of the detector. The coordinate in the z direction indicates the longitudinal position of the
 141 particle along the central axis of the detector, and the angle θ is the polar angle measured with respect to
 142 the central axis of the detector.

143 With this coordinate system, the pseudorapidity η is constructed, as shown in Figure 4, with $\eta = -\ln(\tan(\theta/2))$. Pseudorapidity is used to characterize the deviation angle of a particle with respect to
 144 the central axis of the detector. This variable is widely used because it is nearly relativistically invariant,
 145 making it almost constant regardless of the reference frame used.

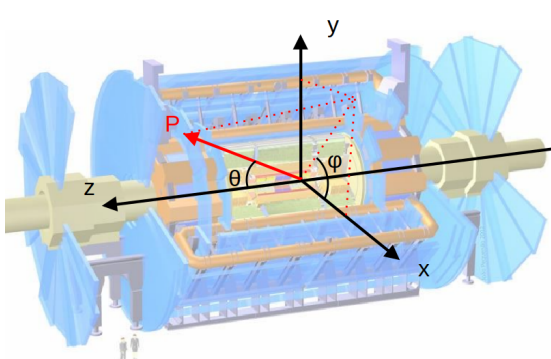


Figure 3: Coordinate system in ATLAS.

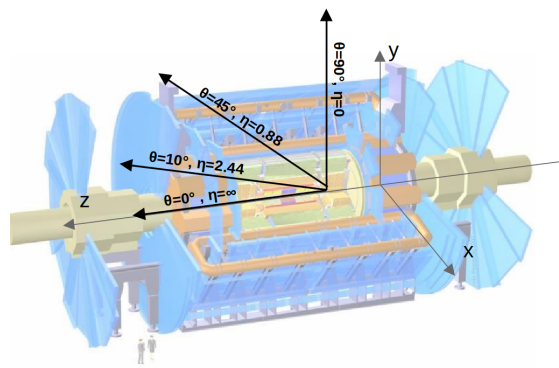


Figure 4: Pseudorapidity η in the (z, y) plan.

147 1.4 Detectors in ATLAS

148 ATLAS is divided into several sub-detectors that measure different properties of particles produced in
 149 proton collisions. As seen in Figure 5, in the (x, y) plane of the detector and in order of distance from the
 150 interaction point, there are ([2] [3]):

- 151 1. The Trajectory Detector (Tracker): This measures the trajectory of charged particles produced in the
 152 collision.
- 153 2. The Electromagnetic Calorimeter (ECal): This measures the energy of electrically charged particles.
- 154 3. The Hadronic Calorimeter (HCAL): This measures the energy of neutral particles and hadrons.
- 155 4. The Muon Detector: Located on the outermost layer, it measures the trajectory of muons, which are
 156 charged particles that easily penetrate through materials

157 1.4.1 Tracker

158 The Tracker is divided into four subparts, as shown in Figure 6.

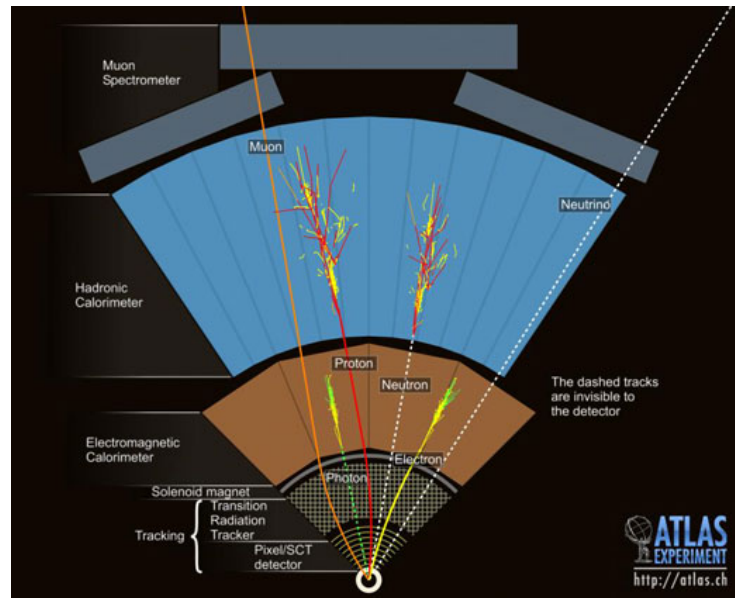


Figure 5: Detectors on the cross-section of the (x, y) plane.

1. **IBL (Insertable B-Layer):** Situated closest to the interaction point of particle beams, the IBL is an additional layer of detectors that was added in 2014 to the existing pixel detector of the LHC to enhance its performance. The main goal of the IBL is to improve the spatial resolution of the existing pixel detectors, which is particularly useful for studying unstable particles, such as heavy quarks like the top quark and Higgs bosons.
2. **Pixel Detector:** Comprising three layers of silicon pixels, the pixel detector is located at distances of 50.5 mm, 88.5 mm, and 122.5 mm from the interaction point. ATLAS's pixel detector has a spatial resolution on the order of a few micrometers, making it the most precise among ATLAS detectors for measuring particle trajectories.
3. **The SCT:** is located at a distance of 30 cm from the interaction point of particle beams at the LHC. It is also designed to precisely measure the trajectories of charged particles produced during the collision of proton beams at the LHC. It is particularly useful for identifying particle decay vertices, measuring transverse momenta, and reconstructing particle jets.
4. **TRT:** The last part of the tracker is a gas detector called TRT (Transition Radiation Tracker). It is also designed to detect and measure the trajectories of charged particles. The TRT is composed of several thousand tubes filled with gas and aligned concentrically around the proton beam. It operates by ionizing the gas as charged particles pass through.

The general characteristics of the Tracker are described in Table 2.

1.4.2 The Electromagnetic and Hadronic Calorimeters

The ATLAS detector is equipped with two types of calorimeters: the ECal and the HCal. The ECal is designed to measure the energy of electromagnetic particles, such as photons and electrons, as well as their

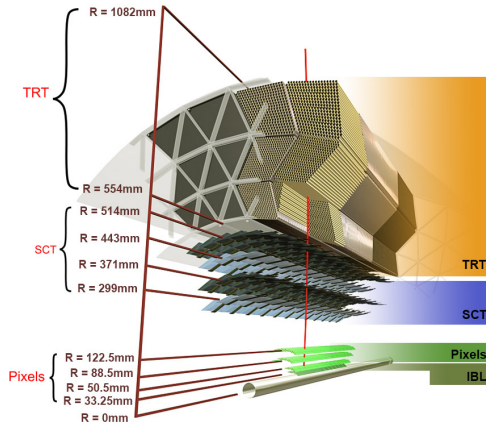


Figure 6: Side view of the tracker.

IBL Radius	32mm ; $r \in [0, 50]$ mm
Pixel Radius	50mm ; $r \in [0, 3000]$ mm
SCT Radius	2990mm ; $r \in [0, 5140]$ mm
TRT Radius	5540mm ; $r \in [0, 10820]$ mm
Tracker z	-721mm ; $z \in [-721, 721]$ mm
Tracker Length	1442mm
Tracker Eta	$2.5 < \eta < 4$

Table 2: Dimensions of the Tracker.

180 electromagnetic showers. It consists of materials that stop these particles and convert their energy into
181 detectable electrical signals.

182 The HCal, on the other hand, is specially designed to measure the energy of hadronic particles, such as
183 protons, neutrons, and charged mesons. It is composed of denser materials capable of stopping hadronic
184 particles and inducing hadronic showers.

185 1.4.3 The Forward Calorimeter

186 The FCal is located in the forward regions of ATLAS, and its spatial characteristics of interest are
187 summarized in Table 3. It consists of three cylindrical modules in the shape of disks, each made up of
188 layers of alternating absorber materials and electrodes. As seen in Figure 7, the first compartment of the
189 FCal is an electromagnetic calorimeter, and the last two are hadronic calorimeters.

190 The absorber materials in the FCal are mainly tungsten and copper, which slow down the particles and
191 cause them to deposit their energy. The readout electrodes are thin copper plates that measure the electric
192 charge created when the particles interact with the absorber material.

FCal Eta	$3.1 < \eta < 4.9$
FCal z	$4.7 \text{ m} < z < 6.2 \text{ m}$

Table 3: Region covered by the FCal.

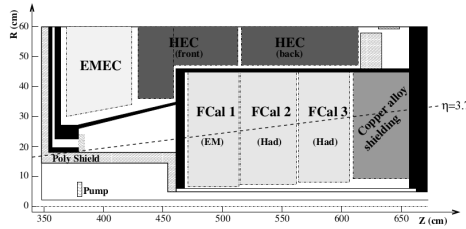


Figure 7: FCal schematic diagram.

193 1.5 The HL-LHC and its Future Detectors

194 During Run 4, ATLAS plans to install new detectors that will enhance its performance in response to
 195 the increased luminosity. The objective of this study is to explore the capabilities offered by these new
 196 detectors, with particular focus on the HGTD [4].

197 1.5.1 The Inner Tracker (ITk) Pixel Detector

198 The ITk Pixel Detector will replace the current Tracker and will possess the same geometrical characteristics.
 199 Offering improved spatial resolution, it also consists of multiple layers of ultra-thin pixels capable of
 200 detecting the electric charges generated by particles as they traverse the detector material.

201 1.5.2 The High Granularity Timing Detector (HGTD)

202 The HGTD is designed to provide state-of-the-art time resolution, enabling precise measurement of the
 203 time of flight of particles produced during proton collisions. This time precision will be used to reduce the
 204 pileup in Run 4 of the LHC, which is expected to be higher than in previous phases.

205 Covering a distant region from the interaction point and being very close to the proton beam, as presented
 206 in Table 4, we will explore in this study if it can also be used for Long-Lived Particle (LLP) searches and
 207 for discrimination of Beam-Induced Background (BIB) traveling collinearly with the beam.

208 The detector consists of two disks with a sensor layer on each side, resulting in a total of 4 sensor layers,
 209 each composed of 2000 LGAD (Low-Gain Avalanche Diode) modules (see Figure 8). These modules,
 210 with dimensions of 20mm \times 40mm, are further subdivided into 450 silicon detection cells of size 1.3mm \times
 211 1.3mm. These cells will measure the signals from ionizing particles passing through the detector. The
 212 signals will be digitized and stored in electronic modules located near the detection cells. Subsequently,
 213 trajectory reconstruction algorithms will be used to extract the position and time of the particles using the
 214 stored signals [5] [6] [7] [8].

215 2 LLPs (Long-Lived Particles)

216 A Long-Lived Particle (LLP) is a particle with a prolonged lifetime, capable of traveling long distances
 217 before decaying into other particles. LLPs are particles with a significantly long lifetime, ranging from
 218 a few nanoseconds to the age of the universe. Such particles can be found in the Standard Model (SM),

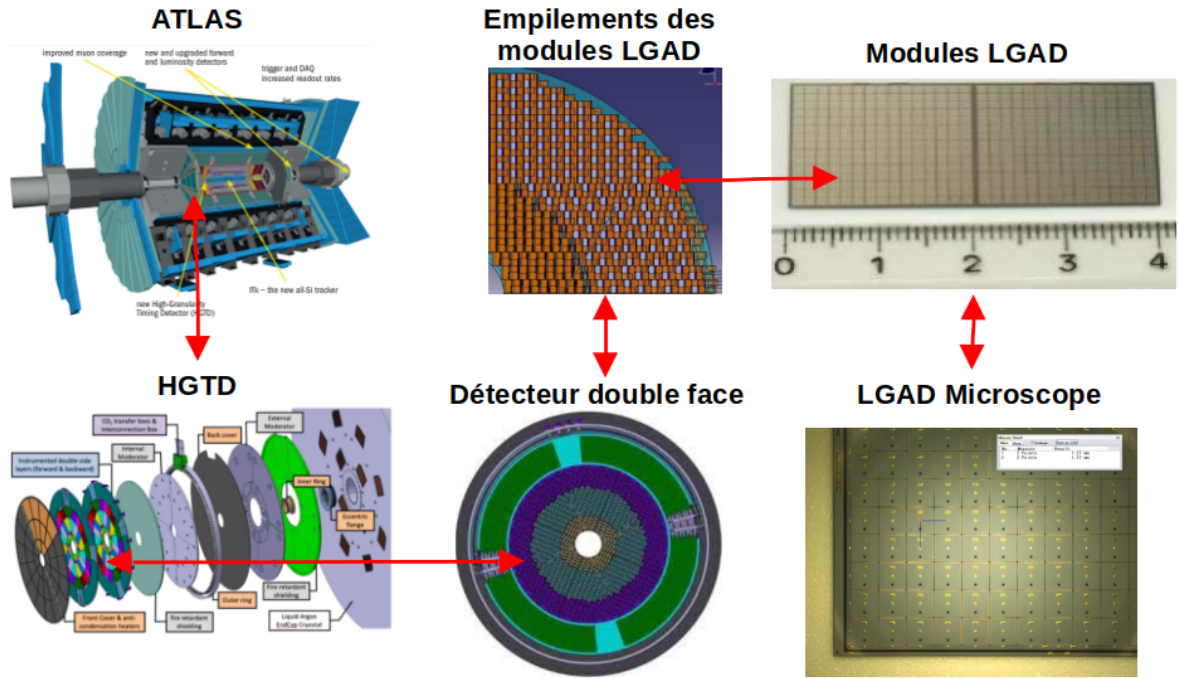


Figure 8: HGTD Detector.

Eta	$2.4 < \eta < 4.0$
z	$3.5 \text{ m} < z < 4.6 \text{ m}$
HGTD Radius	$120 \text{ mm} < r < 640 \text{ mm}$
Sensitive Zone Radius	$110 \text{ mm} < r < 1000 \text{ mm}$
Length	125 mm
Time Resolution	30-50 ps

Table 4: Characteristics of the HGTD.

219 including hadrons like protons and neutrons, as well as leptons like neutrinos and muons. Additionally,
 220 various models of LLPs have been proposed to explain certain mysterious phenomena in particle physics,
 221 such as dark matter, sterile neutrinos, violation of charge-parity (CP) symmetry, and supersymmetry models.
 222

223 To understand why a particle has a long lifetime, we can analyze the parameters that play a role during its
 224 decay. The lifetime $\tau = \frac{1}{\Gamma}$ of a particle can be estimated using what is commonly known as Fermi's Golden
 225 Rule.

226

$$227 \quad \Gamma \propto |M|^2 \times \rho_{(E_F)} \times S$$

228 There are two key parameters to consider. The density of accessible final states $\rho_{(E_F)}$ takes into account
 229 the availability of final states in which the particle can be found after decay. If the number of available final

230 states is low, the probability of decay will be lower. The squared module of the transition amplitude ($|M|^2$)
 231 depends mainly on two factors. These factors are the coupling constant g , which indicates the degree of
 232 interaction between the initial particle and elements of the final state, and the mass of the mediator particle
 233 of the interaction. When the mass of the mediator particle is large compared to the mass of the initial
 234 particle, it means that the energy required to create it is high. Consequently, the probability of interaction
 235 decreases as it is less likely for the initial particle to acquire sufficient energy to produce the mediator
 236 boson and interact with the particles in the final state. An example illustrating this effect is the decay of a
 237 muon into an electron and neutrinos. In this process, the W boson responsible for the interaction has a
 238 mass approximately 1000 times that of the muon. Due to this considerable mass difference, the interaction
 239 between the muon and particles in the final state via the exchange of the W boson is less likely. As a result,
 240 the lifetime of the muon is relatively long.

241

242 For this study, we focus on a reference model of a hidden sector, which is a model used by ATLAS and
 243 CMS to compare their results. It will communicate with the SM through a neutral scalar particle Φ and
 244 will decay via the pathway $\Phi \rightarrow ss \rightarrow f\bar{f}f'\bar{f}'$ as shown in Figure 9. In this model, the long lifetime is
 245 explained by a weak coupling between the scalar and the hidden sector. This scalar will be represented by
 246 the Higgs, with a mass of 125 GeV, as well as other distinct particles ranging from 60 to 1000 GeV. It will
 247 decay into two LLPs, which will also be neutral scalar particles with masses ranging from 5 to 475 GeV,
 248 and these LLPs will further decay into fermions [9].

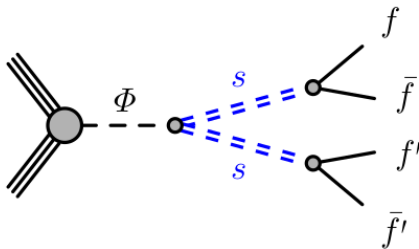


Figure 9: Production of LLP pairs via a scalar Φ .

249 3 Backgrounds for LLP Searches

250 An important part of this study will focus on background reduction in ATLAS with the assistance of HGTD
 251 and the Tracker. Indeed, certain backgrounds have a signal extremely similar to that of a potential LLP,
 252 representing one of the main obstacles in their search.

253 3.1 Different Backgrounds in ATLAS

254 The ATLAS experiment faces six main types of backgrounds. The collisional background arises from
 255 inelastic collisions between particles in the proton beams, producing undesirable secondary particles.
 256 The electromagnetic background is caused by charged particles that can propagate through the detectors
 257 and generate spurious signals. Both of these sources of background constitute what is commonly known
 258 as pileup. The hadronic background can interact with the detector material and produce cascades of

259 secondary particles that may mask signals of interest. The cosmic background comes from cosmic particles
260 originating from space, which can penetrate ATLAS even when the LHC is halted. These particles can
261 mimic signals from particles produced by beam collisions and must be identified and eliminated during
262 data analysis. The instrumental background is generated by the experiment's electronics. Finally, we will
263 particularly focus on the Beam-Induced Background (BIB) for this study.

264

265 **3.2 The Beam-Induced Background (BIB)**

266 The BIB refers to particles and radiation generated during the interaction between the accelerated particle
267 beams of the LHC. This phenomenon is due to several physical processes that occur during the circulation
268 and collision of particle beams. It is one of the most challenging backgrounds to completely reject in
269 LLP studies because the noise it causes is very similar to the signal coming from LLPs. When particle
270 beams circulate in the LHC, they interact with the surrounding environment, leading to the production of
271 secondary particles, including muons, collectively called BIB. It can have several undesirable effects on
272 experiments conducted at the LHC. It can cause disturbances in the particle detectors, produce spurious
273 signals that may mask signals of interest, or introduce systematic errors in measurements. Therefore,
274 understanding and characterizing the BIB is essential to ensure the accuracy of experimental results.

275

276 The BIB can be subdivided into two main components: BIB Gas and BIB Halo. BIB Gas refers to particles
277 and radiation produced by the interaction of particle beams with residual gases present in the accelerator's
278 vacuum tube. When particle beams circulate, they can ionize the molecules of residual gas, creating
279 charged particles such as electrons, positrons, ions, and photons. These particles can be emitted out of
280 the main beam and propagate towards the detectors, contributing to the background noise. On the other
281 hand, BIB Halo refers to particles and radiation produced when particle beams interact with the material
282 constituting the structure of the LHC itself. When proton beams circulate in the LHC, they can interact with
283 collimators, magnets, and other structural elements. These interactions can generate secondary particles
284 that are emitted laterally with respect to the main beam, forming a "halo" of particles around the main
285 beam.

286 **3.3 Pileup**

287 The problem of pileup occurs when multiple proton collisions happen simultaneously, creating a multitude
288 of particles that will interact with the detectors. These particles, which we are not seeking to detect, make
289 it difficult to accurately reconstruct the trajectories and properties of the signals we are interested in. In our
290 case, the pileup will be composed of top quark and anti-quark decays and more generic samples. Pileup
291 will be a major challenge for the HL-LHC experiments and is one of the reasons why HGTD will have such
292 precise time resolution.

293 Part II 294 Appendices

295 4 Signal Study in the HGTD Region

296 In this study, we focus on the analysis of the signal rate, or acceptance, that the three detectors, namely the
 297 tracker, HGTD, and FCal, can receive for a new analysis in the forward region. The signal we are aiming to
 298 detect is produced by the decay of LLPs as described in Chapter 4. The main objective will be to evaluate
 299 the influence of the placement of these detectors on the received signal rate. Indeed, the relative position
 300 of these detectors with respect to the collision region has a significant impact on their ability to detect
 301 and measure the LLPs generated during collisions. A better understanding of the received signal rate will
 302 allow for better planning of their usage in the search for LLPs. We will use several samples of LLPs to
 303 access different masses and lifetimes. We will then extrapolate for each sample to obtain an acceptance
 304 that covers a wide range of lifetimes.

305 4.1 The Samples

306 For the samples, we relied on the article [9]. This study, which we heavily relied upon, presents an analysis
 307 of the decay of LLPs produced in pairs using proton-proton collision data collected by the ATLAS detector,
 308 particularly the ECal and HCal, between 2015 and 2018. The results show that the observed event numbers
 309 are consistent with the expected background, allowing for the establishment of limits for different reference
 310 signals, including the Standard Model Higgs boson and scalars of various masses. During this study, they
 311 created a series of Monte Carlo samples to simulate the decay process of different scalar particles into two
 312 LLPs. The different scalars are characterized by different masses, 125 GeV, 400 GeV, 600 GeV, and 1000
 313 GeV. Here, we used these different samples to parameterize our code and then focused on the analysis of
 314 the scalar at 125 GeV representing the Higgs.

315

316 For the Higgs decay, we had access to four different masses of LLPs, namely 55 GeV, 35 GeV, 16 GeV, and
 317 5 GeV. Each of these masses has distinct characteristics, including different lifetimes, which allow us to
 318 understand the influence of mass on the detected signal rate while representing a fairly complete spectrum
 319 of LLPs that can be produced by the Higgs decay. Additionally, except for the one at 16 GeV, we have two
 320 different lifetimes, namely "low" and "high," for each mass of LLPs. The lifetimes for each of the samples,
 321 here represented as decay lengths $c\tau$, therefore depend on the mass for which they will be detected. They
 322 are chosen with the objective of decaying in the hadronic calorimeter beyond any theoretical considerations
 323 to facilitate the study and can be changed later using a weighting method.

324 4.2 Calculation of Acceptance for Different Samples

325 Here, by acceptance, we mean the number of particles decaying within the region covered by the Tracker,
 326 HGTD, and FCal detectors, compared to the total number of particles produced.

$$327 \text{Acceptance} = \frac{\text{Number of particles detected in the detectors' region}}{\text{Total number of particles}}$$

328 The choice was made for these detectors because their η values are similar, allowing us to utilize the
 329 reduction of BIB by HGTD in the region covered by these three detectors. To calculate the acceptance, we
 330 considered the z position and η value of each detector. Specifically, we considered the tracker with an η
 331 range from 2.4 to 4 and a z position range from 0.8 m to 3.5 m. Additionally, since the HGTD and FCal
 332 detectors have similar spatial characteristics, we treated them as one detector, with an η range from 2.4 to 4
 333 and a z position range from 3.5 m to 6.2 m.

334 To evaluate the acceptance of these detectors in a specific region, we used a simple spatial rejection. By
 335 applying values of η and position (z) corresponding to the specified range for each detector, we could
 336 isolate the region of interest and obtain the number of particles detected in that region. By counting the
 337 number of particles detected in the specified region for each detector, we can calculate the detector's
 338 acceptance in that region. Acceptance is defined as the ratio of the number of detected particles to the
 339 total number of particles present in the region. Table 7 shows the results obtained for the 7 samples. The
 340 acceptance column in η represents the rate of detected particles if only a rejection on η is applied, while
 341 the last two columns represent the acceptance for rejections in both η and z.

m_H 125 GeV	$c\tau$ (m)	Acceptance in η (%)	Tracker (%) 0.8 m \leq z \leq 3.5 m	HGTD/FCal (%) 3.5 m \leq z \leq 6.2 m
m_S 55 GeV High	5.32	25.28	0.26	0.17
m_S 55 GeV Low	1.05	25.23	2.69	0.83
m_S 35 GeV High	2.63	11.85	0.09	0.05
m_S 35 GeV Low	1.31	11.92	0.21	0.15
m_S 16 GeV High	0.58	7.71	0.14	0.08
m_S 5 GeV High	0.41	7.06	0.03	0.03
m_S 5 GeV Low	0.13	7.16	0.19	0.10

Table 5: Acceptance of the two LLPs for different masses and positions.

342 4.3 Weighting Formula

343 To modify the distribution of samples according to their lifetime, we use a formula that calculates a weight
 344 for each event. This weight is then used to recompute the new distributions of these events.

345 The formula used to calculate the distribution of samples with different lifetimes is as follows.

$$346 w(t) = \frac{\tau_{gen}}{\exp(-t/\tau_{gen})} \cdot \frac{\exp(-t/\tau_{new})}{\tau_{new}}$$

347 In this formula, τ_{gen} represents the lifetime of the samples as indicated in the table, while τ_{new} is the new
 348 desired lifetime. The first term in the equation is used to smooth our exponential curve, while the second
 349 term redistributes the samples. This allows us to modify the distributions of the samples according to the
 350 desired new lifetime.

351 4.4 Acceptance for Different Lifetimes

352 The calculation of the new distributions is done for a $c\tau$ ranging from 10^{-4} to 10^2 meters. For each
 353 new lifetime, we use the method described earlier. The resulting acceptance for the Tracker and for the
 354 HGTD/FCal is shown in Figures 33 and 34.

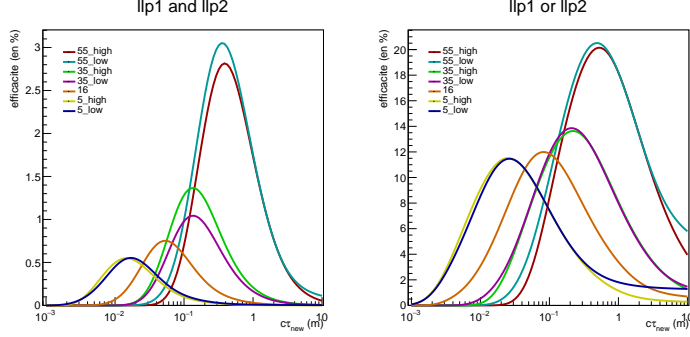


Figure 10: Variation of the acceptance for the tracker as a function of the decay distance ($c\tau$) for a pair of LLPs on the left or a single LLP on the right.

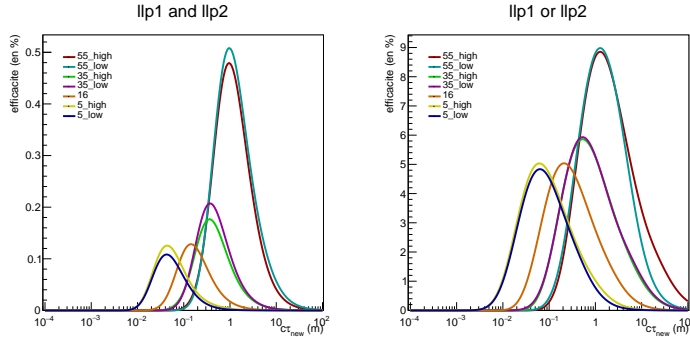


Figure 11: Variation of the acceptance for the HGTD/FCal as a function of the decay distance ($c\tau$) for a pair of LLPs on the left or a single LLP on the right.

355 The left graphs represent the probability that both LLPs decay within the detector, while the right graph
 356 represents the probability of only one LLP being detected. As the signal signature is more easily detectable
 357 when both LLPs are present, the left graphs will be of greater interest to us. We can observe that for large
 358 values of lifetime, the graphs behave strangely. This is due to the weighting becoming approximate for
 359 large values of $c\tau$.

360 4.5 Analysis of Results

361 The graphs in Figure 35 and 36 provide information on the fractions of LLP signal that will be available for
 362 analysis in the forward region, where the HGTD could reduce background noise. The presented curves
 363 delimit the already accessible regions. The green band represents the region that we can exploit for the
 364 35 GeV LLPs. We observe that by using these detectors, we are able to cover a slightly shorter range of
 365 lifetimes compared to previous analyses.

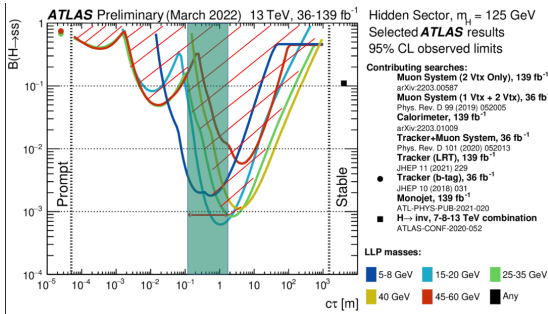


Figure 12: Region accessible with the Tracker.

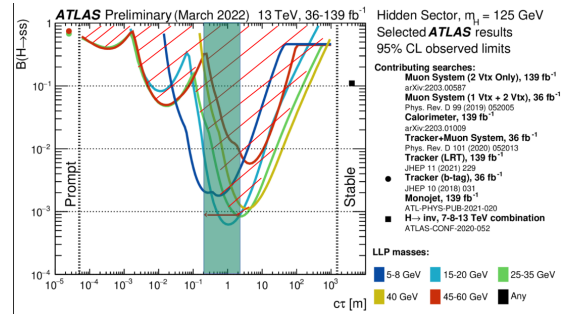


Figure 13: Region accessible with HGTD/FCal.

Part III

BIB Rejection

5 Objective

The main objective of this study is to analyze to what extent we can use the HGTD to reject the background noise caused by the Beam Induced Background (BIB). As a reminder, the BIB samples we use come from only one side of the LHC, so we will have an asymmetry in our analysis. However, since the HGTD is symmetrically placed on both sides of the interaction point, we can extrapolate our results to both sides. The method we will adopt consists of reconstructing the paths traveled by the particles from the hits, using a specialized data clustering library. Then, we will use a specific parameter, adjusted using a linear fit, to determine if these trajectories correspond to jets or to BIB. We will proceed as follows: create an initial clustering with the Anti-KT algorithm, refine the clustering using the DBSCAN algorithm, perform a fit on each cluster using the Minuit library, and analyze the data based on the fit result.



Figure 14: Five main steps for BIB rejection.

This method is not applicable in all cases. Indeed, with our method, we can only reject BIB events that have a direction opposite to the Standard Model jet. Therefore, we have three different cases, as shown in Figure 15.
The first case (in blue) is when the BIB only affects HGTD A. This situation represents 77% of the total hits in our sample, and our rejection method can be used without any problem. The second case (in green) represents approximately 14% of the hits and occurs when the BIB affects both HGTDs. Here, we can use our method to reject hits in HGTD A and, by using the tracker, we could trace back to the entire track and

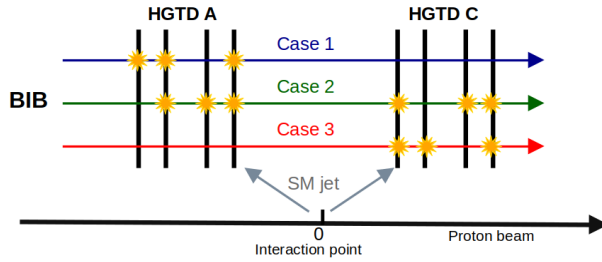


Figure 15: Three different cases.

385 reject it. The third case is when the BIB only affects HGTD C, representing approximately 9% of the hits,
386 and we cannot perform rejection with our method. Other approaches for rejection will be presented later.

387 **Aside:** With the samples we are using, we can see that the time when the BIB events and the interaction
388 point events hit the HGTD is different, about -11 ns for BIB and $+11$ ns for the top. We might naively
389 believe that we could use this information for rejection. However, this is an effect of the simulation; in
390 reality, during data taking, the internal clock of the LHC reboots every 2.5 ns. Therefore, we cannot use
391 this effect during data taking, and we will not use it here.

392 6 Athena, the Software of ATLAS

393 Athena is the software used in the ATLAS experiment. It serves several purposes, such as trajectory
394 reconstruction, particle identification, and the search for new particles through missing energy analysis. In
395 our case, we will use it to study the deposits left by BIB and top events in the HGTD. The Athena code is
396 hosted on the CERN GitLab service. Primarily written in C++, it consists of thousands of subprojects
397 linked together through compilation and building mechanisms, ensuring the coherence and interoperability
398 of the entire code but making code navigation and management complex.
399

400 The main use we made of Athena in this study is the reconstruction of hits on detectors from particle
401 samples. For this, we use events generated by Monte Carlo methods and then simulate their interactions
402 with the detectors using Geant4 to obtain data in HITS format, as shown in Figure 17.

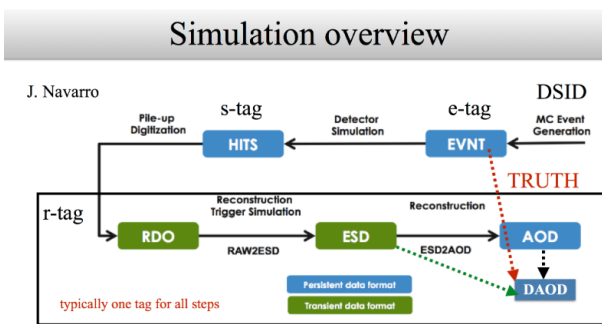


Figure 16: Simulation and reconstruction process.

403 7 Simulation Steps

404 In Figure 17, we can see three major steps in the simulation of samples. The first step is the creation
 405 of events, which involves particles with characteristics similar to those found in the LHC. This step is
 406 represented by an EVNT file. The second step is the simulation of hits on the detectors, which represents
 407 the output of the detection materials before the signal is processed. The last step, designated by the AOD
 408 format, represents the signal after it has undergone initial processing through the LHC electronics and is
 409 stored for future analyses.

410

411 To simulate our samples, we used the s-tag reconstruction with the Géant4 s4038 geometry. Once we
 412 obtained our data in HITS format, we needed to transform the coordinates using SiHitAnalysis to make
 413 them usable. During the simulation in HITS format, the coordinates obtained for each hit are internal to
 414 each LGAD module, as seen in Figure 8. We also needed to obtain the PDG index, which indicates whether
 415 a hit obtained by reconstruction comes from a real particle or from another process, such as instrumental
 416 noise. Thus, each hit is associated with a number corresponding to the particle that deposited energy. If
 417 the number is -9999.0, it means that the hit does not come from a particle. For an unknown reason, the
 418 reconstruction produced a considerable number of hits not associated with real particles, approximately
 419 87%. It is important to understand that this index, along with a few other variables that we will explain
 420 later, is accessible only because we are using simulation data. In real data acquisition, we would not have
 421 access to this information in advance. These pieces of information are crucial for us to validate our results
 422 afterward, but they should not be used in advance to obtain these results.

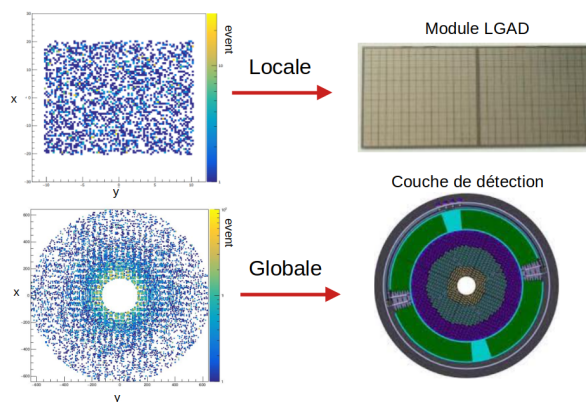


Figure 17: Transformation from local to global coordinates.

423 The entire process of simulation and conversion is explained in the paper "Simulation_s4038.pdf" avail-
 424 able with this document or on the following GitHub link: "<https://gitlab.cern.ch/lreynaud/background-education-with-hgtd>"

426 7.1 Available Variables

427 The HITS format provides us access to certain variables for each hit, and we will list them here, with an
 428 example shown in Figure 18.

- 429 • **barcode:** Internal to Géant4, allows tracking the evolution of a particle.

- 430 • **barrel/endcap**: Indicates whether the hit is in the barrel or endcap, not relevant with HGTD as all
431 hits are in the endcap.
- 432 • **layer/disk**: Indicates the layer of the detector where the hit occurred.
- 433 • **eloss**: Energy deposited during the hit
- 434 • **module eta**: Module of the variable eta, $|\eta|$
- 435 • **module phi**: Module of the variable phi, $|\phi|$
- 436 • **r**: The radius of the hit in mm (0 being the interaction point).
- 437 • **time**: Temporal position of the hit in ns.
- 438 • **step**: Internal to Géant4, linked to the barcode information.
- 439 • **x**: x-position of the hit in mm.
- 440 • **y**: y-position of the hit in mm.
- 441 • **z**: z-position of the hit in mm.

442 With the addition of the PDG index, other variables become accessible, but as mentioned earlier, these
443 are not variables that we should use in the "amons" (initial stages) of our study because they will not be
444 available in the HITS format during data taking. We can only use them to verify our results.

- 445 • **eta**: Eta position of the hit.
- 446 • **pT**: Momentum of the hit.
- 447 • **pdgid**: PDG index to determine the nature of the particle that produced the hit.
- 448 • **phi**: Phi position of the hit.
- 449 • **prodVtx_x**: x-coordinate of the production vertex.
- 450 • **prodVtx_y**: y-coordinate of the production vertex.
- 451 • **prodVtx_z**: z-coordinate of the production vertex.

452 As shown in Figure 18, the list of variables available with ROOT for HGTD contains valuable information
453 that can be used to validate our results. However, it's important to remember that some of these variables,
454 especially those related to the production vertex, may not be accessible during data taking and should not
455 be relied upon for real-time analysis.

456 8 Samples

457 For our analysis of BIB rejection, we used three types of samples: one for simulating the BIB, one for
458 simulating top decays, and another for simulating generic events from the Standard Model.



Figure 18: Example of a list of variables with ROOT for HGTD.

459 8.1 BIB Samples

460 For the BIB, we used events generated through Monte Carlo simulation using the FLUKA software, which
 461 specializes in simulating particle and nucleus interactions and transport in matter. This sample represents
 462 BIB particles that traverse the LHC in the counterclockwise direction. Subsequently, we performed a
 463 simulation of events with the detector to obtain the corresponding interactions.

464 There are four types of BIB samples, two from the "beam gas" with energies of 20 MeV and 20 GeV, and
 465 two from the "beam halo" also with energies of 20 MeV and 20 GeV.

466 The names of the used samples are as follows:

```
467 mc15_13TeV.309680.BeamHaloGenerator_BeamGasB1_20MeV.evgen.EVNT.e6513
468 mc15_13TeV.309682.BeamHaloGenerator_BeamGasB1_20GeV.evgen.EVNT.e6513
469 mc15_13TeV.309681.BeamHaloGenerator_BeamHaloB1_20MeV.evgen.EVNT.e6513
470 mc15_13TeV.309683.BeamHaloGenerator_BeamHaloB1_20GeV.evgen.EVNT.e6513
```

471 8.2 Top Samples

472 For the top samples, we used events created in another study, which we reconstructed using GEANT4
 473 simulation. These samples represent the decay of a top quark or antiquark from the interaction point of
 474 the proton beams. We then used the same method as with the BIB to simulate the interaction with the
 475 detector.

476 *EVNT_ttbar.32468304._002312.pool.root.1*

477 8.3 Minbias Samples

478 For the generation of generic pileup events, we used samples specifically produced by ATLAS for this
 479 purpose. There are two types of minbias samples, one with low energy and the other with high energy,
 480 which we will mix manually in a certain proportion.

481 *mc15_14TeV.800380.Py8EG_A3NNPDF23LO_minbias_inelastic_low_keepJets.evgen.EVNT.e8205*
 482 *mc15_14TeV.800381.Py8EG_A3NNPDF23LO_minbias_inelastic_high_keepJets.evgen.EVNT.e8205*

483

484 8.4 Visualization

485 Once these samples are combined, we obtain a situation described in Figure 19, where the HGTD is
 486 represented by its 4 detection layers.

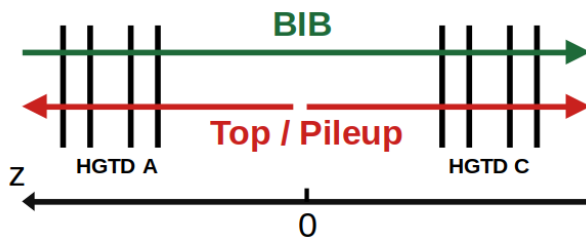


Figure 19: Schema of the different sample.

487 9 Final Samples

488 The purpose of this section is to create a sample of several events that faithfully reproduces the events that
 489 will be recorded by the HGTD during the run 4.

490 We have three different samples that we will mix together: a BIB sample, itself composed of a mixture
 491 of "beam halo" and "beam gas" events with energies of 20 MeV and 20 GeV respectively, totaling
 492 approximately 3000 non-empty events; a top decay sample with 1000 non-empty events; and two pileup
 493 samples, one with 20,000 events at low energy and the other with 2000 events at high energy.

494 The mixing of the samples, as represented in Figure 21, will be done as follows:

495 A function will randomly choose one BIB event and one top event and mix them together. Then, we will
 496 add a certain number of pileup events (we will try different numbers of events, ranging from 0 to 200). For
 497 each pileup event, a random function will determine whether we add a low-energy event or a high-energy
 498 event according to a proportion of 99.65% low-energy events and 0.35% high-energy events.

499 We can choose the number of events per sample, and for the rest of this study, we will use samples of 400
 500 events each.

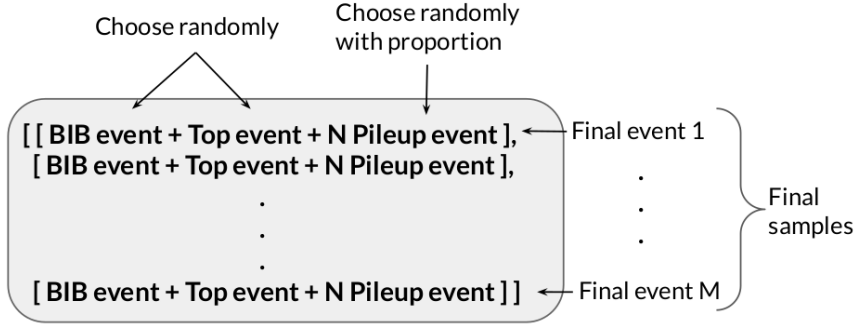


Figure 20: Final sample.

501 10 Clustering with Anti-KT

502 10.1 The Energy-Momentum Four-Vector

503 The first clustering will be done using the Anti-KT algorithm with the python library FastJet. Anti-KT is
 504 a clustering algorithm that mainly relies on two parameters: the energy-momentum four-vector P and a
 505 spatial radius r . We need to obtain the four-vectors using the variables at our disposal, which will require
 506 some approximations. The variables available to us are: time, position, and energy deposited in each hit.
 507

508 To obtain the momentum, we use the following formula:

$$509 \quad \vec{P} = \frac{m \times d}{t}$$

510 where m is the mass of the particle (assumed to be the mass of a proton), d is the distance traveled by the
 511 particle from the interaction point, and t is the time taken by the particle to travel that distance.
 512

513 The energy-momentum four-vector is then given by:

$$514 \quad P = (E, \vec{P})$$

515 where E is the energy deposited in the hit.

516 To obtain the momentum, we use the following formula:

$$517 \quad \vec{P} = \frac{m \times d}{t}$$

518 where m is the mass (which we approximate to 1), d is the distance traveled from the interaction point to the
 519 position of the hit, and t is the time taken. We then obtain a result that needs to be converted into natural units.
 520

521 For the total energy, we use the approximation $E_{\text{tot}} = \text{eloss}$, which means the energy deposited by the hit.
 522 It involves several approximations, but it works quite well!

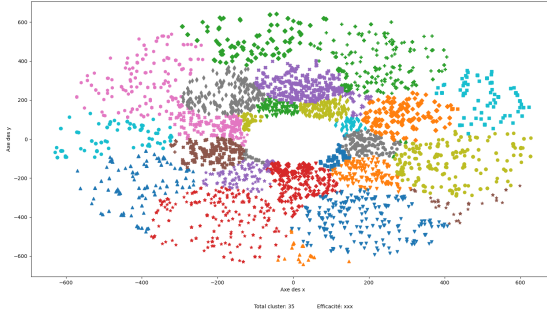


Figure 21: Graphical representation of a cluster in the (x, y) plane using Anti-KT.

523 10.2 The Optimal Radius

524 We know that ATLAS uses the Anti-KT algorithm with a radius of 0.4 for clustering. Here, we will try to
 525 determine if this radius is suitable for our study. To find the optimal radius, we will use two parameters that
 526 we want to optimize. These parameters are:

- 527 • **The number of hits included in our cluster:** We perform clustering on all hits, but some hits may
 528 not belong to any cluster and become isolated. This happens particularly when the radius is small.
 529 However, we hope to differentiate as many hits as possible, so the number of isolated hits should be
 530 minimized.
- 531 • **The number of well-differentiated clusters:** After clustering, we want to perform a linear fit, and
 532 knowing the direction of the jet, we want to be able to differentiate the jet, i.e., determine whether it
 533 belongs to the BIB or to a top/pileup event. If the clustering radius is too large, we will mix too
 534 many different trajectories into our clusters, and the fit will be more likely to be incorrect. This part
 535 will be described in more detail in the sections on "Linear Fit" and "Analysis."

536 We will iterate over several values of the radius and choose the one that optimizes these two parameters the
 537 best.

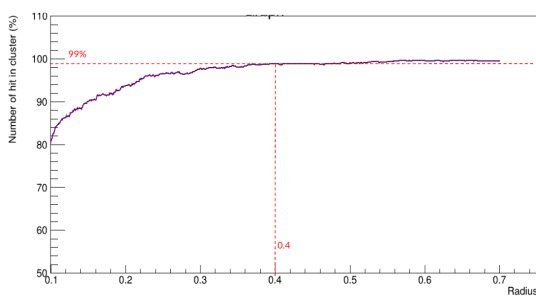


Figure 22: Rate of hits included in the clustering.

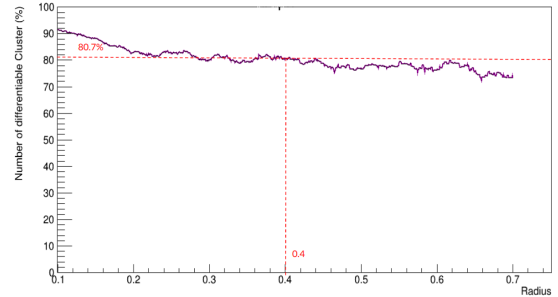


Figure 23: Clustering efficiency in differentiation.

538 From the graph on the right, we can see that starting from a value of 0.4, the rate of hits included in the
 539 clusters reaches 99% and remains almost constant. The differentiation rate remains fairly constant at
 540 around 81% between 0.23 and 0.43, despite some statistical variations. Therefore, we can conclude that the
 541 optimal radius for clustering with Anti-KT is between 0.4 and 0.43, and we will choose 0.4 for the rest of
 542 this study to align with ATLAS.

543 11 Clustering with DBSCAN

544 11.1 Reason for a second clustering

545 Although clustering with Anti-KT is quite effective, achieving around 80% of correctly differentiated
 546 clusters, it does not take into account certain information that could easily improve its efficiency. This is the
 547 case with temporal data. Let's take an example of a cluster of BIB particles represented in Figure 24. The
 548 list shows the times of different hits, and all these hits form a cluster. However, we can easily see that there
 549 are actually three different particles in this cluster, represented by the three colors red, blue, and green.

```

[-10.731889724731445, -10.69443130493164, -10.630202293395996,
-11.531757354736328, -11.447617530822754, -11.531797409057617,
-11.447623252868652, -10.334186553955078, -10.259435653686523]

```

Figure 24: Collection of hits forming a cluster, hits are represented by their time in nanoseconds.

550 The idea here is to perform a second temporal clustering with DBSCAN within each cluster created by
 551 Anti-KT with a radius of 0.4 to separate the jets that have the same energy-momentum four-vector and
 552 spatial location, but have different times.

553 11.2 DBSCAN

554 DBSCAN is an algorithm that uses two main parameters: *epsilon* for the radius and *min_samples* for the
 555 minimum number of hits required to create a cluster. *min_samples* will be fixed at 2 for the rest of this
 556 study, and we will use the same method as with Anti-KT to determine an optimal radius.

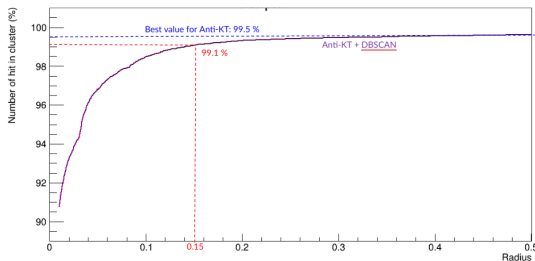


Figure 25: Rate of hits included in the clustering.

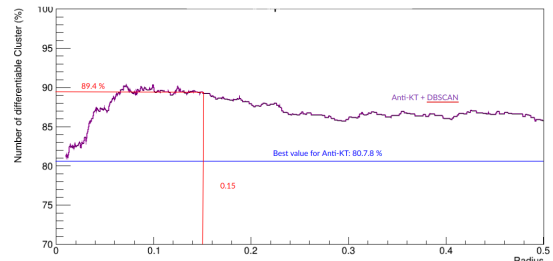


Figure 26: Clustering efficiency for differentiation.

557 In the violet line on the graphs of Figure 25 and 26, we can see the results of our clustering with Anti-KT +
 558 DBSCAN, and in the blue line, the results we had when using only Anti-KT with a radius of 0.4.

559 For a radius of 0.15, we can observe an improvement in differentiation of around 10% while losing less
 560 than 0.5% of hits. The choice of the radius here is somewhat arbitrary, and we could have chosen a slightly
 561 larger radius that isolates fewer hits but gives us a lower efficiency. However, it is not a problem to isolate a
 562 certain number of hits if it mainly affects top/pileup events, which is the case here.

563 12 Linear Fit with Minuit

564 The objective here is to perform a linear fit on each of the clusters produced by Anti-KT and DBSCAN. We
 565 will perform a fit of the form:

566
$$t = az + b$$

567 The sign of a should give us the direction of propagation of the cluster along the z axis, allowing us to
 568 determine whether it is a BIB event or a top/pileup event. If $a > 0$, it corresponds to events coming from
 569 the interaction point, and if $a < 0$, it corresponds to BIB events. Figure 27 and 28 illustrates how the fit is
 570 constructed around a cloud of points and what sign of a is expected based on the origin of the cluster.

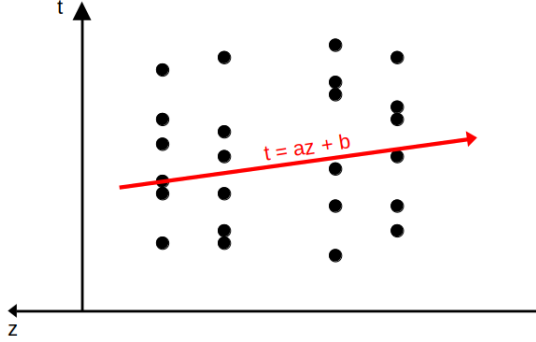


Figure 27: Linear fit of a cluster.

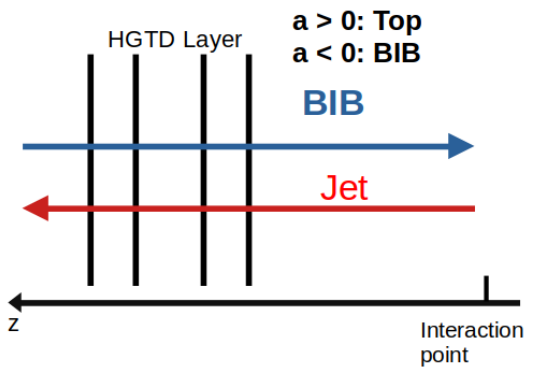


Figure 28: Sign of a according to the propagation direction.

571 To perform this fit, we will use the Python library **Minuit**. Minuit uses the method of least squares, and its
 572 operation for a linear fit is quite simple. For a cluster of n points, it will seek to find the parameters a and b
 573 for which the following function is minimized:

574
$$\sum_{i=0}^n (t_i - az_i - b)^2$$

575 We will also need to initialize our parameters, and for this, we will choose $a = 0.01$ and $b = 0$. a represents
 576 the inverse of a velocity, and if we were trying to fit four more or less aligned points (one point per layer),
 577 we would expect to find something close to the inverse of the speed of light (in mm per ns). However,
 578 since it is a cloud of points, the fit is not exact, and we cannot use this point directly. Nevertheless, most
 579 of the time, we will find $a < 0.01$. b indicates the time (in ns) at which the particles reach the first layer.
 580 This time fluctuates between -10 nanoseconds for BIB and 10 nanoseconds for events coming from the
 581 interaction point.

582 Once the least squares method is used, Minuit also provides us with a covariance matrix. This matrix
 583 indicates the reliability of the fit. We did not have time to explore it in our study, but from a distance, we
 584 noticed that fits with a parameter a that has a large variance, for example, such that $(|a| - \text{var}(a)) < 0$,
 585 have a high chance of making a bad prediction (about 60% of bad predictions compared to 10% for other
 586 cases). This method of using variance is, of course, very rudimentary and only indicates that the variance
 587 is larger than our value. A more thorough study could be conducted to determine from which values we
 588 could choose to reject the fit.

589 13 Analysis

590 The analysis will be done quite simply using a confusion matrix. With the linear fit, we predicted which
 591 samples our clusters belonged to. We will then check if the prediction is correct for each of our clusters
 592 and arrange them as shown in the table in Figure 29.

Sample	BIB	Top
$a > 0$	B1	T1
$a < 0$	B2	T2
total	B3	T3

■ B2 and T1 are the number of BIB and top clusters that we manage to differentiate.
■ B1 and T2 are the number of BIB and top clusters that we wrongly differentiate.

Figure 29: Cluster differentiations.

593 In the table, the rows represent the predictions, and the columns represent the true results. B1 and B2
 594 represent our BIB clusters, with B1 being those we mistakenly identified as top clusters and B2 being those
 595 we correctly differentiated, and vice versa for T1 and T2.

596 After verifying all our clusters, we can construct a confusion matrix using the method described in Figure
 597 30.

True positive %	$100 \times B2/B3$	→ True positive is the rate of BIB well differentiate.
False positive %	$100 \times T2/T3$	→ False positive is the rate of top/pileup differentiate as BIB.
True negative %	$100 \times B1/B3$	→ True negative is the rate of BIB differentiate as top.
False negative %	$100 \times T1/T3$	→ False negative is the rate of top/pileup well differentiate.

Figure 30: Confusion matrix.

598 14 Results

599 An analysis will be performed for different numbers of pileup, namely 0, 10, 25, 50, 100, 150, and 200. For
 600 each of these numbers, we will produce 500 samples. As mentioned in the section **Final Samples**, each
 601 sample consists of 400 final events randomly generated. We then perform clustering and analysis on each
 602 of the samples. A summary of this part is presented in Figure 32.

603 The results obtained for certain numbers of pileup are displayed in Table 6 and in the graph.

604 We can observe from the blue and green bars that BIB (Beam-Induced Background) is not affected by the
 605 presence of pileup. It originates from a different source than top and pileup events, and Anti-KT can easily
 606 isolate it.

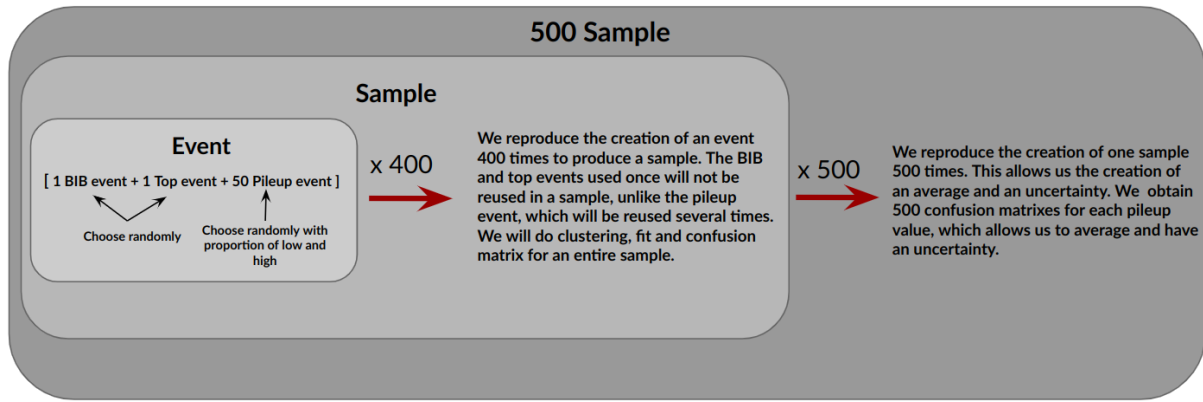


Figure 31: Analysis of the samples.

Pileup per event	0	50	100	200
True positive %	$89.6 \pm 2.5\%$	$90.0 \pm 2.4\%$	$89.8 \pm 2.3\%$	$89.8 \pm 2.3\%$
False positive %	$6.0 \pm 0.2\%$	$14.2 \pm 0.2\%$	$15.1 \pm 0.2\%$	$15.9 \pm 0.2\%$
True negative %	$10.4 \pm 2.5\%$	$10.0 \pm 2.4\%$	$10.3 \pm 2.5\%$	$10.2 \pm 2.3\%$
False negative %	$94.0 \pm 0.2\%$	$85.8 \pm 0.2\%$	$84.4 \pm 0.2\%$	$84.1 \pm 0.2\%$

Table 6: Matrice de confusion pour 0, 50, 100, 200 événements pileup.

607 The SM (Standard Model) jets, on the other hand, are more sensitive to the presence of pileup, causing a
 608 disturbance with a small number of pileup events. The efficiency loss is around 8% when adding 50 pileup
 609 events, but it undergoes minimal changes beyond that point.

610 15 Conclusion

611 The main objective was to conduct a preliminary study to determine if the HGTD could contribute to
 612 reducing BIB (Beam-Induced Background) and, consequently, aid in the search for LLP (Long-Lived
 613 Particles). The method used involved several approximations that could be improved, such as the creation
 614 of the energy-momentum quadrivector, finding an ideal radius for DBSCAN, or the simulation of the
 615 samples themselves, which seems to generate too many "false results".

616

617 However, we can still conclude that such a method can be effective in rejecting BIB, and the HGTD has
 618 the potential to become a relevant tool in the search for LLP in the long term. Further refinements in the
 619 approach and improvements in the simulation and clustering techniques could enhance the performance
 620 and accuracy of the results. This study provides a promising starting point and opens up avenues for future
 621 investigations and advancements in the search for LLP using the HGTD technology. This report, along
 622 with all the documents related to the project, is accessible on the following GitLab repository:

623 <https://gitlab.cern.ch/lreynaud/background-eduction-with-hgtd>

624 Here's a brief presentation of the different documents you will find there:

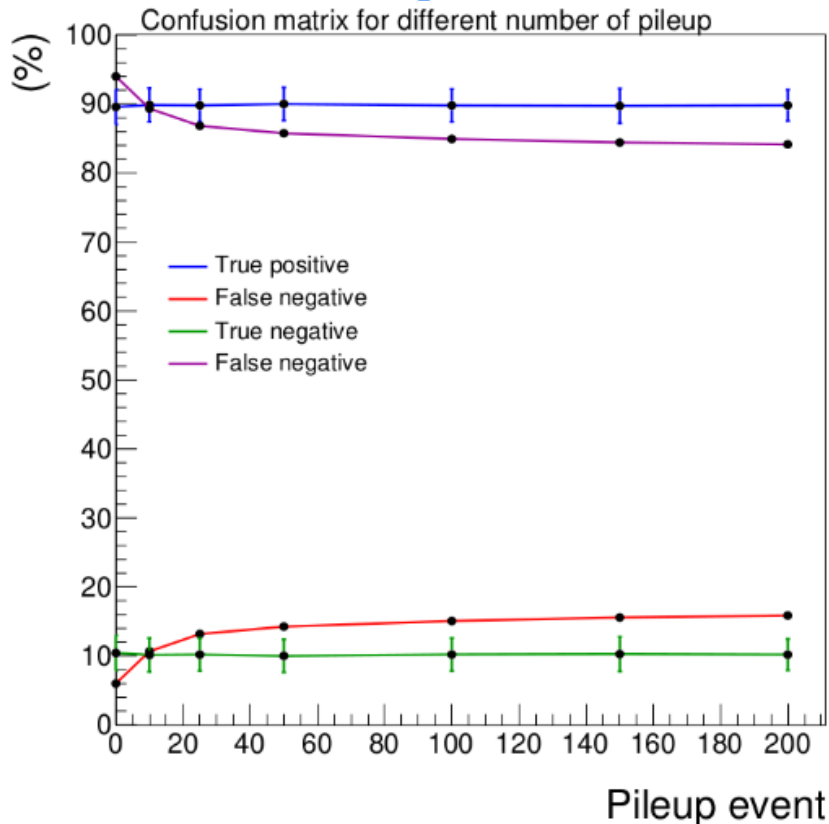


Figure 32: Results for 0, 10, 25, 50, 100, 150, and 200 pileup events.

- **Background_reduction_with_HGTD.pdf:** This is the report you are currently reading, available in both French and English.
- **Présentation_background_reduction_with_HGTD.pdf:** It consists of a series of slides that present this project.
- **Simulation_s4038.pdf:** A small document explaining how to perform a reconstruction s4038 and how to convert local coordinates to global ones.
- **Simulation_s4038.txt:** The accompanying file with the code for the reconstruction, which can be copied and pasted from there.
- **fast.py:** The main script of the code.
- **fast_library.py:** The main library used by the script fast.py.
- **fast_tools_library.py:** A secondary library for small functions used during the analysis.
- **fast_ClusterGraph.py:** A script to display clusters graphically.
- **fast_GraphConfusionMatrix.py:** A script used to analyze and graphically display data created by fast.py and stored in txt format.
- **Help_simulation_s4038.py:** A script that enables faster preparation of simulations.

- **Help_SiHitAnalysis.py:** A script that enables faster preparation of coordinate transformations.
- **Help_root_fusion.py:** A script that enables faster merging of root files.

640 • **Help_SiHitAnalysis.py:** A script that enables faster preparation of coordinate transformations.
641 • **Help_root_fusion.py:** A script that enables faster merging of root files.
642 If you need any further assistance or have any questions about these documents or the project, feel free to
643 ask!

644 **leo.auguste@protonmail.com**

645 Part IV

646 Appendices

647 16 Signal Study in the HGTD Region

648 In this study, we focus on the analysis of the signal rate, or acceptance, that the three detectors, namely the
 649 tracker, HGTD, and FCal, can receive for a new analysis in the forward region. The signal we are aiming to
 650 detect is produced by the decay of LLPs as described in Chapter 4. The main objective will be to evaluate
 651 the influence of the placement of these detectors on the received signal rate. Indeed, the relative position
 652 of these detectors with respect to the collision region has a significant impact on their ability to detect
 653 and measure the LLPs generated during collisions. A better understanding of the received signal rate will
 654 allow for better planning of their usage in the search for LLPs. We will use several samples of LLPs to
 655 access different masses and lifetimes. We will then extrapolate for each sample to obtain an acceptance
 656 that covers a wide range of lifetimes.

657 16.1 The Samples

658 For the samples, we relied on the article [9]. This study, which we heavily relied upon, presents an analysis
 659 of the decay of LLPs produced in pairs using proton-proton collision data collected by the ATLAS detector,
 660 particularly the ECal and HCal, between 2015 and 2018. The results show that the observed event numbers
 661 are consistent with the expected background, allowing for the establishment of limits for different reference
 662 signals, including the Standard Model Higgs boson and scalars of various masses. During this study, they
 663 created a series of Monte Carlo samples to simulate the decay process of different scalar particles into two
 664 LLPs. The different scalars are characterized by different masses, 125 GeV, 400 GeV, 600 GeV, and 1000
 665 GeV. Here, we used these different samples to parameterize our code and then focused on the analysis of
 666 the scalar at 125 GeV representing the Higgs.

667

668 For the Higgs decay, we had access to four different masses of LLPs, namely 55 GeV, 35 GeV, 16 GeV, and
 669 5 GeV. Each of these masses has distinct characteristics, including different lifetimes, which allow us to
 670 understand the influence of mass on the detected signal rate while representing a fairly complete spectrum
 671 of LLPs that can be produced by the Higgs decay. Additionally, except for the one at 16 GeV, we have two
 672 different lifetimes, namely "low" and "high," for each mass of LLPs. The lifetimes for each of the samples,
 673 here represented as decay lengths $c\tau$, therefore depend on the mass for which they will be detected. They
 674 are chosen with the objective of decaying in the hadronic calorimeter beyond any theoretical considerations
 675 to facilitate the study and can be changed later using a weighting method.

676 16.2 Calculation of Acceptance for Different Samples

677 Here, by acceptance, we mean the number of particles decaying within the region covered by the Tracker,
 678 HGTD, and FCal detectors, compared to the total number of particles produced.

$$679 \text{Acceptance} = \frac{\text{Number of particles detected in the detectors' region}}{\text{Total number of particles}}$$

680 The choice was made for these detectors because their η values are similar, allowing us to utilize the
 681 reduction of BIB by HGTD in the region covered by these three detectors. To calculate the acceptance, we
 682 considered the z position and η value of each detector. Specifically, we considered the tracker with an η
 683 range from 2.4 to 4 and a z position range from 0.8 m to 3.5 m. Additionally, since the HGTD and FCal
 684 detectors have similar spatial characteristics, we treated them as one detector, with an η range from 2.4 to 4
 685 and a z position range from 3.5 m to 6.2 m.

686 To evaluate the acceptance of these detectors in a specific region, we used a simple spatial rejection. By
 687 applying values of η and position (z) corresponding to the specified range for each detector, we could
 688 isolate the region of interest and obtain the number of particles detected in that region. By counting the
 689 number of particles detected in the specified region for each detector, we can calculate the detector's
 690 acceptance in that region. Acceptance is defined as the ratio of the number of detected particles to the
 691 total number of particles present in the region. Table 7 shows the results obtained for the 7 samples. The
 692 acceptance column in η represents the rate of detected particles if only a rejection on η is applied, while
 693 the last two columns represent the acceptance for rejections in both η and z.

m_H 125 GeV	$c\tau$ (m)	Acceptance in η (%)	Tracker (%) 0.8 m \leq z \leq 3.5 m	HGTD/FCal (%) 3.5 m \leq z \leq 6.2 m
m_S 55 GeV High	5.32	25.28	0.26	0.17
m_S 55 GeV Low	1.05	25.23	2.69	0.83
m_S 35 GeV High	2.63	11.85	0.09	0.05
m_S 35 GeV Low	1.31	11.92	0.21	0.15
m_S 16 GeV High	0.58	7.71	0.14	0.08
m_S 5 GeV High	0.41	7.06	0.03	0.03
m_S 5 GeV Low	0.13	7.16	0.19	0.10

Table 7: Acceptance of the two LLPs for different masses and positions.

694 16.3 Weighting Formula

695 To modify the distribution of samples according to their lifetime, we use a formula that calculates a weight
 696 for each event. This weight is then used to recompute the new distributions of these events.

697 The formula used to calculate the distribution of samples with different lifetimes is as follows.

$$698 w(t) = \frac{\tau_{gen}}{\exp(-t/\tau_{gen})} \cdot \frac{\exp(-t/\tau_{new})}{\tau_{new}}$$

699 In this formula, τ_{gen} represents the lifetime of the samples as indicated in the table, while τ_{new} is the new
 700 desired lifetime. The first term in the equation is used to smooth our exponential curve, while the second
 701 term redistributes the samples. This allows us to modify the distributions of the samples according to the
 702 desired new lifetime.

703 **16.4 Acceptance for Different Lifetimes**

704 The calculation of the new distributions is done for a $c\tau$ ranging from 10^{-4} to 10^2 meters. For each
 705 new lifetime, we use the method described earlier. The resulting acceptance for the Tracker and for the
 706 HGTD/FCal is shown in Figures 33 and 34.

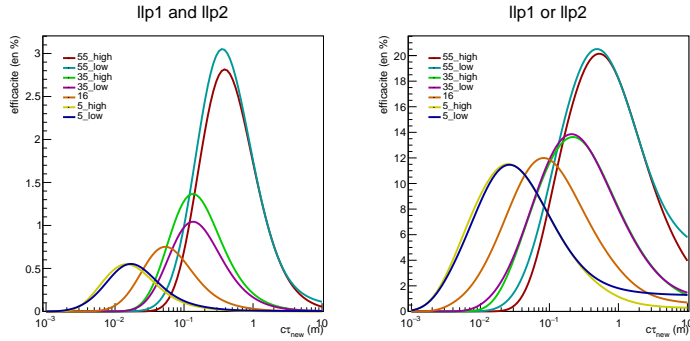


Figure 33: Variation of the acceptance for the tracker as a function of the decay distance ($c\tau$) for a pair of LLPs on the left or a single LLP on the right.

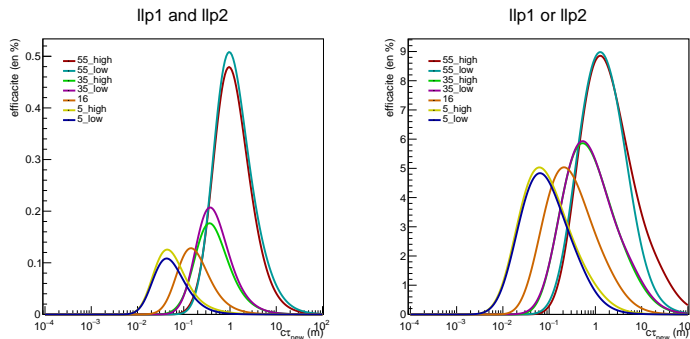


Figure 34: Variation of the acceptance for the HGTD/FCal as a function of the decay distance ($c\tau$) for a pair of LLPs on the left or a single LLP on the right.

707 The left graphs represent the probability that both LLPs decay within the detector, while the right graph
 708 represents the probability of only one LLP being detected. As the signal signature is more easily detectable
 709 when both LLPs are present, the left graphs will be of greater interest to us. We can observe that for large
 710 values of lifetime, the graphs behave strangely. This is due to the weighting becoming approximate for
 711 large values of $c\tau$.

712 **16.5 Analysis of Results**

713 The graphs in Figure 35 and 36 provide information on the fractions of LLP signal that will be available for
 714 analysis in the forward region, where the HGTD could reduce background noise. The presented curves
 715 delimit the already accessible regions. The green band represents the region that we can exploit for the
 716 35 GeV LLPs. We observe that by using these detectors, we are able to cover a slightly shorter range of
 717 lifetimes compared to previous analyses.

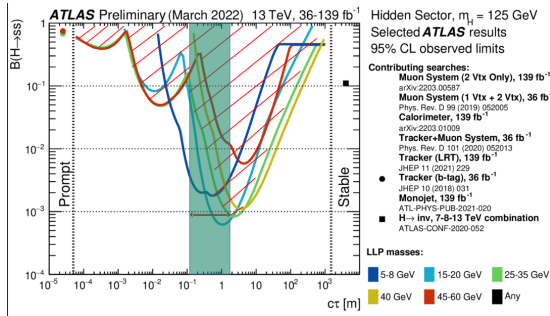


Figure 35: Region accessible with the Tracker.

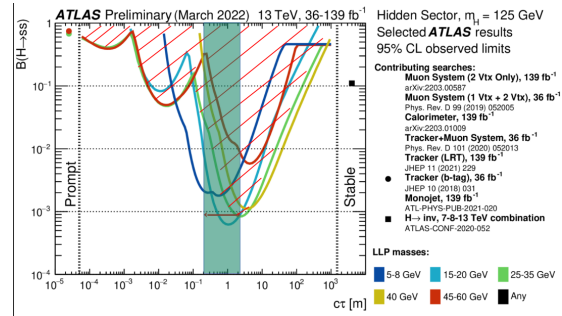


Figure 36: Region accessible with HGTD/FCal.

References

- [1] L. D. (de Physique de Clermont), *The search for exotic long-lived particles: illuminating a blind spot of the LHC programme*, Cambridge HEP Seminar (2022) (cit. on p. 4).
- [2] T. A. Collaboration, *The ATLAS Experiment at the CERN Large Hadron Collider*, Journal of Instrumentation (2008), URL: <https://dx.doi.org/10.1088/1748-0221/3/08/S08003> (cit. on p. 7).
- [3] T. A. Collaboration, *Technical Design Report for the Phase-II Upgrade of the ATLAS Trigger and Data Acquisition System*, (2018), URL: <https://cds.cern.ch/record/2285584/files/ATLAS-TDR-029.pdf> (cit. on p. 7).
- [4] A. G. ; B. A. I. ; B. O. ; F. P. ; L. M. ; R. L. ; T. L., *High-Luminosity Large Hadron Collider (HL-LHC) : Technical Design Report V. 0.1*, CERN Yellow Reports: Monographs (2017), URL: <https://cds.cern.ch/record/2284929> (cit. on p. 10).
- [5] o. b. o. t. A. H. G. M.P. Casado, *A High-Granularity Timing Detector for the ATLAS Phase-II upgrade*, Nuclear Inst. and Methods in Physics Research, A (2022), URL: <https://www.sciencedirect.com/science/article/pii/S0168900222002005> (cit. on p. 10).
- [6] C. G. T. L. experiments Committee ; LHCC, *Technical Design Report: A High-Granularity Timing Detector for the ATLAS Phase-II Upgrade*, ATLAS Collaboration (2020), URL: <https://cds.cern.ch/record/2719855> (cit. on p. 10).
- [7] O. b. o. t. H. g. sha Mallik, *A High Granularity Timing Detector (HGTD) for the ATLAS Experiment at LHC, CERN*, The University of Iowa (2018), URL: <https://cds.cern.ch/record/2320566/files/ATL-LARG-SLIDE-2018-297.pdf> (cit. on p. 10).
- [8] M. Alshamsi, *The ATLAS High Granularity Timing Detector*, University Of Sharjah (), URL: <https://cds.cern.ch/record/2651090/files/hgtd-2.pdf> (cit. on p. 10).

- 748 [9] T. A. Collaboration, *Search for neutral long-lived particles in pp collisions at $\sqrt{s} = 13$ TeV that decay*
749 *into displaced hadronic jets in the ATLAS calorimeter*, (2022),
750 URL: <https://arxiv.org/abs/2203.01009> (cit. on pp. 12, 14, 31).